

The strong modulation limit of excitons and trions in moiré materials

Yongxin Zeng and Allan H. MacDonald

Department of Physics, University of Texas at Austin, Austin, TX 78712

(Dated: October 4, 2021)

The optical properties of weakly-doped two-dimensional materials are dominated by strong exciton and trion absorption and luminescence features. In this article we examine the influence of moiré patterns in semiconductor heterobilayers on exciton and trion states in the limit of strong moiré modulation potentials, commenting on similarities and differences compared to the case of excitons and trions in semiconductor quantum dots. We discuss strategies for using optical properties as quantitative probes of moiré materials, and the prospects for exploiting moiré materials to design unique light emitters.

I. INTRODUCTION

Moiré superlattices form when two-dimensional (2D) crystals are stacked with a small twist angle or lattice mismatch. When the host materials are semiconductors or semimetals, moiré superlattices are accurately described by continuum models with the periodicity of the moiré pattern, giving rise to artificial two-dimensional moiré materials with controllable large lattice constants. Extensive theoretical and experimental work on twisted bilayer graphene [1–22] and twisted bilayer transition metal dichalcogenides (TMDs) [23–37] over the past several years has established moiré materials as an important platform for studies of strongly correlated electron physics.

In addition to modifying low-energy electronic properties, the moiré potentials in twisted bilayer TMDs also significantly modify interband excitonic collective modes, and associated optical properties [38–53]. The moiré modulation splits both intralayer and interlayer excitonic peaks in the optical spectrum into a series of subpeaks and modifies optical selection rules. Since the electrons, holes, and excitons are often strongly localized near minima of the periodic moiré potential, moiré superlattice systems can act as a new and more perfectly periodic realization of quantum dot arrays [39, 40], and be used to engineer single-photon emitters and entangled photon sources [43, 48] with potential applications in quantum optics.

Theories of the excitonic properties of moiré materials have progressed by treating excitons as point particles moving in a periodic moiré potential [38–40]. Recent numerical and experimental studies show that moiré modulation strengthens when strain is taking into account [54–57], and that the conduction band electrons and valence band holes that combine to form excitons in a moiré material can be attracted to different lateral positions within the moiré pattern [58–62], distorting the excitonic modes. In the strong modulation limit, the electron and hole moiré band widths become extremely small and the moiré material can be viewed as an accurately periodic array of quantum dots. In this article we study how strong confinement and lateral shifts between the electron and hole confining centers affect the properties of excitons

and trions in the quantum dot array limit of a moiré material. In Sec. II we introduce our model for electrons and holes in a moiré superlattice, and present results for Coulomb interaction matrix elements in the single-particle harmonic oscillator basis that we use for numerical calculations. In Secs. III and IV we calculate the ground state energies and optical absorption strengths of excitons and trions respectively, by exact diagonalization (ED) of the corresponding few-body Hamiltonians in the harmonic oscillator basis. Finally, in Sec. V we discuss the implications of our results, and point to future work that can be approached with our method. We find that the optical properties of systems in which electrons and holes are trapped at the same position within the periodic moiré pattern are very different from those of systems in which electrons and holes are trapped at different positions; the former case is distinguished by fewer but stronger absorption features because of the approximate applicability of angular momentum conservation selection rules. Magnetic fields are potentially useful in characterizing moiré materials, but because of the strong electron-hole binding in two-dimensional material excitons and trions will yield substantial corrections that can be used to identify electron, hole, exciton, and trion configurations only at very strong magnetic fields.

II. THE MODEL

In a TMD heterobilayer moiré superlattice, electrons and holes tend to localize at one of three high-symmetry sites in a moiré unit cell [54–62] at which the local stacking places the metal atoms of one layer above either metal, chalcogen, or empty sites of the layer below. As summarized in Fig. 1, there is an important distinction between the case in which electrons and hole are localized at the same positions in the moiré pattern or at different positions. It is not yet confidently known which among the various TMD heterobilayer systems fall into the former category and which fall into the latter category. When the electron and hole sites are the same, they form a triangular lattice of sites at which excitons can be localized. When the electron and hole sites are separated in the 2D plane, however, their triangular lattices combine to form a hexagonal lattice like the one shown

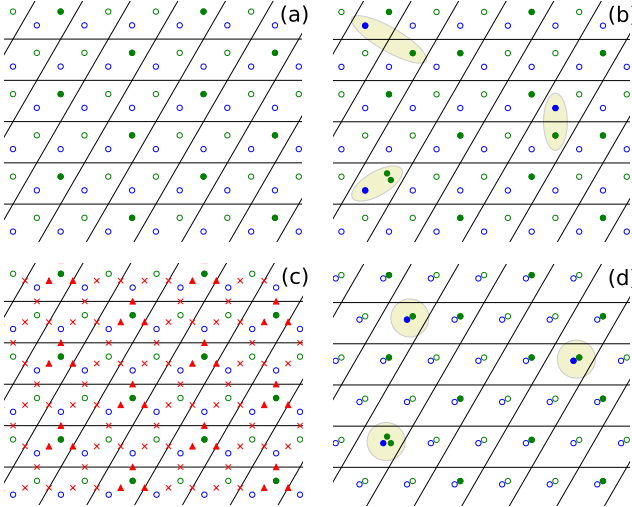


FIG. 1. (a) A hole-doped moiré superlattice at filling factor $\nu = 1/3$. The blue and green circles represent the electron and hole confining centers respectively, which are assumed here to be located at different high-symmetry stacking sites. The filled and empty circles distinguish sites that are occupied by a quasiparticle from those that are empty. The doped holes form a Wigner crystal in the ground state. (b) The moiré lattice with some electron-hole excitations. The yellow ellipses show three different types of electron-hole excitations: an exciton (right), a trion (lower left), and an example of a more widely separated electron-hole pair (top left). (c) If the center of an electron site and its neighboring hole site is associated with an exciton or trion excitation, as marked by the red crosses and triangles, together they form a kagome lattice. (d) Same as (b), except that the electrons and holes are localized at the same sites. The yellow circles show two excitons and a trion excitation.

in Fig. 1(a). In a hole-doped system some of the hole sites are occupied, and at certain fractional fillings the ground state of the doped holes is a lattice Wigner crystal [24–26, 36]. Fig. 1 shows an example at filling factor $\nu = 1/3$. Possible low-energy excitations of the system include electron-hole pairs at empty neighboring sites (an exciton), or an electron-hole pair at a filled hole site and its neighboring electron site (a trion). Excitations with electrons and holes farther away are also possible, but have higher energies and weaker optical absorptions. If we ignore these, and consider only near-neighbor exciton and trion excitations, each bond between an electron site and its neighboring hole site can be associated with a possible exciton or trion excitation (marked by red crosses and triangles in Fig. 1(c)), depending on whether the hole site is occupied or not. Together these excitations form a kagome lattice. Excitons and trions on different sites are coupled by intersite hopping of their constituents, and via Coulomb interactions. We do not account for these complications here.

In this article we consider both two-particle exciton and three-particle trion electron-hole complexes, ignoring the possible role of coupling to other excitations of

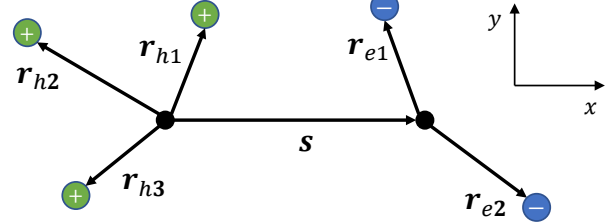


FIG. 2. Schematic illustration of the model system – a few electrons and holes confined in a 2D quantum dot. The black dots stand for the confining potential minima for electrons and holes, and the blue and green dots represent electrons and holes respectively. The vectors \mathbf{r}_{ei} and \mathbf{r}_{hj} are defined relative to the potential minima for electrons and holes respectively, which are separated by the vector $\mathbf{s} = s\hat{x}$ when the electrons and holes are in the same layer and by $s\hat{x} + d\hat{z}$ when the electrons and holes are in layers separated by distance d .

the system. We study a system of N_e electrons and N_h holes confined in a 2D quantum dot (Fig. 2) with harmonic confining potentials for the electrons and holes, and a magnetic field $\mathbf{B} = B\hat{z}$ applied perpendicular to the 2D plane. We consider the general case in which the electrons and holes have different effective masses m_e and m_h and are localized at different lateral positions in the same or different layers by confining potentials that can have different oscillator frequencies ω_e and ω_h . For heterobilayer moiré superlattices, states with electrons and holes in the same layer are relevant in absorption or reflection measurements and states with electrons and holes in different layers are relevant in luminescence experiments. The system is described by Hamiltonian

$$H = H_e + H_h + V_{ee} + V_{hh} + V_{eh}. \quad (1)$$

The electron and hole single-particle terms are

$$H_e = \sum_{i=1}^{N_e} \left[\frac{(\mathbf{p}_{ei} + e\mathbf{A}_e(\mathbf{r}_{ei}))^2}{2m_e} + \frac{1}{2}m_e\omega_e^2 r_{ei}^2 \right], \quad (2)$$

$$H_h = \sum_{j=1}^{N_h} \left[\frac{(\mathbf{p}_{hj} - e\mathbf{A}_h(\mathbf{r}_{hj}))^2}{2m_h} + \frac{1}{2}m_h\omega_h^2 r_{hj}^2 \right], \quad (3)$$

where i and j are labels for electrons and holes, and the origins of \mathbf{r}_e and \mathbf{r}_h are chosen to be at the minima of the corresponding confining potentials. We choose a gauge such that $\mathbf{A}_e(\mathbf{r}_e) = \frac{1}{2}\mathbf{B} \times \mathbf{r}_e$ and $\mathbf{A}_h(\mathbf{r}_h) = \frac{1}{2}\mathbf{B} \times \mathbf{r}_h$, i.e., the symmetric gauge, but with different origins for

electrons and holes. The interaction terms are

$$V_{ee} = \sum_{i_1 < i_2}^{N_e} \frac{e^2}{\epsilon |\mathbf{r}_{ei_1} - \mathbf{r}_{ei_2}|}, \quad (4)$$

$$V_{hh} = \sum_{j_1 < j_2}^{N_h} \frac{e^2}{\epsilon |\mathbf{r}_{hj_1} - \mathbf{r}_{hj_2}|}, \quad (5)$$

$$V_{eh} = \sum_{i=1}^{N_e} \sum_{j=1}^{N_h} \frac{-e^2}{\epsilon \sqrt{|\mathbf{r}_{ei} - \mathbf{r}_{hj}|^2 + \mathbf{s}^2 + d^2}}, \quad (6)$$

where \mathbf{s} is the displacement between the confining potential minimum of electrons and holes. We choose the coordinate axes such that the 2D crystals are in the \hat{x} - \hat{y} plane and the in-plane component of \mathbf{s} is along the \hat{x} direction (see Fig. 2). d is the distance between the electron and hole layers ($d = 0$ when the electrons and holes are in the same layer), and ϵ is the dielectric constant of the dielectric surrounding the system. The most commonly employed surrounding dielectric is hexagonal boron nitride (hBN), which has an anisotropic dielectric tensor. In this case $\epsilon = \sqrt{\epsilon_{zz}\epsilon_{\perp}}$ and the effective layer separation d is related to the physical separation d_0 by $d = d_0\sqrt{\epsilon_{\perp}/\epsilon_{zz}}$, where ϵ_{\perp} and ϵ_{zz} are respectively the perpendicular-to-plane and in-plane components of the dielectric tensor.

We diagonalize the few-particle Hamiltonian using a

configuration interaction approach with basis state Slater determinants constructed from the eigenstates of H_e and H_h . Our calculations are similar to those reported in earlier papers [63–66] on quantum dots in semiconductor quantum wells, except that we consider here the possibility that the electrons and holes are localized at different lateral positions. The harmonic oscillator eigenstates $|n_+n_-\rangle$ are labelled by two quantum numbers n_+ and n_- , with energy eigenvalues

$$E_{n_+n_-} = (n_+ + \frac{1}{2})\hbar\Omega_+ + (n_- + \frac{1}{2})\hbar\Omega_-, \quad (7)$$

where $\Omega_{\pm} = \Omega \pm \omega_c/2$ with $\Omega = \sqrt{\omega^2 + (\omega_c/2)^2}$ and $\omega_c = eB/m$. (See Appendix A for derivations.) To diagonalize the Hamiltonian we choose basis states that are antisymmetrized combination of electron-hole many particle product states

$$|n_{e1}n_{e1-}, n_{e2}n_{e2-}, \dots; n_{h1}n_{h1-}, n_{h2}n_{h2-}, \dots\rangle. \quad (8)$$

Antisymmetrization is not required between electrons or holes since these can be considered to be distinguishable. The two-particle matrix elements for Coulomb interactions are evaluated by expanding the interactions in terms of ladder operators of the single-particle basis. For interactions among electrons or holes, the result is

$$\langle n'_{1+}n'_{1-}, n'_{2+}n'_{2-} | V_{\alpha\alpha} | n_{1+}n_{1-}, n_{2+}n_{2-} \rangle = \frac{\sqrt{\beta_{\alpha}}}{2} \frac{e^2}{\epsilon l_B} \left(\prod_{i\lambda} n'_{i\lambda}! n_{i\lambda}! \right)^{1/2} (-1)^{n'_{1+}+n_{1-}+n'_{2+}+n_{2-}} \delta_{l'l} \times \sum_{k_{i\lambda}=0}^{\min(n'_{i\lambda}, n_{i\lambda})} \left(\prod_{i\lambda} \frac{(-1)^{k_{i\lambda}} 2^{-p}}{k_{i\lambda}!(n'_{i\lambda} - k_{i\lambda})!(n_{i\lambda} - k_{i\lambda})!} \right) \cdot \Gamma(p + \frac{1}{2}), \quad (9)$$

where $\alpha = e, h$, the sums define separate factors for $\lambda = \pm$ and particle $i = 1, 2$, the conserved angular momentum quantum numbers $l = n_{1+} - n_{1-} + n_{2+} - n_{2-}$ and $l' = n'_{1+} - n'_{1-} + n'_{2+} - n'_{2-}$, and $p = \sum_{i\lambda} (n'_{i\lambda} + n_{i\lambda} - 2k_{i\lambda})/2$. In Eq. (9), the magnetic length $l_B = \sqrt{\hbar/eB}$ and we have defined $\beta_{\alpha} = \sqrt{1 + (2\omega_{\alpha}/\omega_{\alpha c})^2}$.

The two-particle matrix elements of V_{eh} are similar but do not conserve angular momentum because the electron and hole oscillators have different centers in general:

$$\langle n'_{e+}n'_{e-}, n'_{h+}n'_{h-} | V_{eh} | n_{e+}n_{e-}, n_{h+}n_{h-} \rangle = -\sqrt{\frac{\beta_{eh}}{2}} \frac{e^2}{\epsilon l_B} \left(\prod_{\alpha\lambda} n'_{\alpha\lambda}! n_{\alpha\lambda}! \right)^{1/2} (-1)^{n'_{e+}+n_{e-}+n'_{h+}+n_{h-}} \times \sum_{k_{\alpha\lambda}=0}^{\min(n'_{\alpha\lambda}, n_{\alpha\lambda})} \left(\prod_{\alpha\lambda} \frac{(-1)^{k_{\alpha\lambda}} (\frac{\beta_{eh}}{\beta_{\alpha}})^{\frac{1}{2}(n'_{\alpha\lambda}+n_{\alpha\lambda}-k_{\alpha\lambda})}}{k_{\alpha\lambda}!(n'_{\alpha\lambda} - k_{\alpha\lambda})!(n_{\alpha\lambda} - k_{\alpha\lambda})!} \right) \cdot I, \quad (10)$$

where $\beta_{eh} = \beta_e\beta_h/(\beta_e + \beta_h)$, and the (n', n, k) -dependent integral

$$I = \int_0^{\infty} d\tilde{q}^2 e^{-\tilde{q}^2} (\tilde{q}^2)^{p-\frac{1}{2}} e^{-\tilde{q}\tilde{d}} \cdot \int_0^{2\pi} \frac{d\phi}{2\pi} (ie^{i\phi})^{l-l'} e^{i\tilde{q}\tilde{s} \cos \phi}, \quad (11)$$

where we introduced the dimensionless lengths $\tilde{d} = \frac{\sqrt{2\beta_{eh}}}{l_B} d$, $\tilde{s} = \frac{\sqrt{2\beta_{eh}}}{l_B} s$, the total angular momentum quantum numbers $l = n_{e+} - n_{e-} - n_{h+} + n_{h-}$, $l' = n'_{e+} - n'_{e-} - n'_{h+} + n'_{h-}$, and $p = \sum_{\alpha\lambda} (n'_{\alpha\lambda} + n_{\alpha\lambda} - 2k_{\alpha\lambda})/2$. The radial

part of the integral in Eq. (11) can be computed analytically and we obtain

$$I = 4^{-p} \Gamma(2p+1) \int_0^{2\pi} \frac{d\phi}{2\pi} (ie^{i\phi})^{l-l'} U(p + \frac{1}{2}, \frac{1}{2}, \frac{1}{4}(\tilde{d} - i\tilde{s} \cos \phi)^2), \quad (12)$$

where U is the confluent hypergeometric function of the second kind. The angular integral must be evaluated numerically for $s \neq 0$. For $s = 0$,

$$I(s=0) = \delta_{l'l} \cdot 4^{-p} \Gamma(2p+1) U(p + \frac{1}{2}, \frac{1}{2}, \frac{\tilde{d}^2}{4}). \quad (13)$$

When $d \rightarrow 0$, $I(s=0) \rightarrow \delta_{l'l} \Gamma(p + \frac{1}{2})$. More detail on the derivations of these formulas is provided in Appendix A. The generalization of these formulas to properly anti-symmetrized multi-particle states basis with spin and/or valley degrees of freedom is straightforward.

III. EXCITONS

We first consider the case of excitons – two-particle states with an electron and a hole that are distinguishable. We neglect intervalley exchange interactions [67–70] so that the excitonic states are valley independent. The i th eigenstate of the Hamiltonian can be written as

$$|\Psi_{eh}^{(i)}\rangle = \sum_{n_e n_h} C_{n_e n_h}^{(i)} |n_e; n_h\rangle, \quad (14)$$

where n_e is a shorthand for the two indices (n_{e+}, n_{e-}) that specify which electron basis state is occupied, and similarly for n_h . The coefficients $C_{n_e n_h}^{(i)}$ are obtained by numerical diagonalization of the Hamiltonian in the magnetic harmonic oscillator basis $|n_e; n_h\rangle$. In our model, exciton energies are given relative to the band gap between potential extrema.

In the weak-confinement limit, the relative-motion electron-hole pair state is very weakly distorted, and the electron-hole center-of-mass moves in a weak modulation potential. The characteristic length scale for bound electron-hole pairs is the effective Bohr radius $a_B^* = \hbar^2/m\epsilon^2$ where $m = m_e m_h / (m_e + m_h)$ is the reduced mass of the electron-hole pair. The characteristic energy scale is the effective Rydberg $Ry^* = e^2/2\epsilon a_B^* = m\epsilon^4/2\epsilon^2 \hbar^2$. In our calculations we set $m_e = 0.4m_{e0}$, $m_h = 0.5m_{e0}$ where m_{e0} is the free electron mass, and $\epsilon = 5$, as approximate parameters for intralayer excitons in bilayer TMDs [71] surrounded by hBN. Then we find $a_B^* = 1.19$ nm and $Ry^* = 121$ meV.

In the strong-confinement and large- s limit, the electron and hole are each confined in a harmonic potential, with length scale given by the oscillator length $l_\alpha = \sqrt{\hbar/m_\alpha \omega_\alpha}$ and energy scale $\hbar\omega_\alpha$. The magnetic field provides another length scale, the magnetic length $l_B = \sqrt{\hbar/eB}$, and another energy scale, the cyclotron energy $\hbar\omega_{ac} = \hbar e B / m_\alpha$. For our explicit calculations we

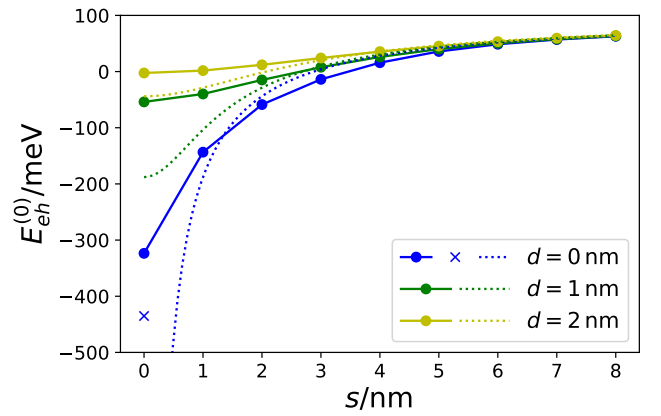


FIG. 3. Ground-state exciton energy $E_{eh}^{(0)}$ as a function of the in-plane separation between the electron and hole confining potential minima s , for intralayer (blue $d = 0$) and interlayer (green and yellow $d = 1, 2$ nm) excitons. These results were calculated at magnetic field $B = 10$ T, but differ very little from results calculated at $B = 0$. The dots and solid lines are numerical results from ED calculations, and the dotted curves are the large- s approximation of (15). The blue cross shows the weak-confinement approximation (16) expression which adds a zero-point confinement energy to the free exciton energy.

choose $\hbar\omega_e = \hbar\omega_h = 50$ meV. Then the harmonic confinement lengths $l_e = 1.95$ nm and $l_h = 1.75$ nm. At magnetic field $B = 10$ T, the magnetic length $l_B = 8.11$ nm is considerably longer and the cyclotron energies $\hbar\omega_{ec} = 2.9$ meV, $\hbar\omega_{hc} = 2.3$ meV considerably smaller than other length and energy scales. In a magnetic field, the oscillator length $L_\alpha = \sqrt{\hbar/m_\alpha \Omega_\alpha}$ with $\Omega_\alpha = \sqrt{\omega_\alpha^2 + (\omega_{ac}/2)^2}$. We therefore see that due to the large effective masses in the TMDs, the oscillator length is weakly perturbed by a $B = 10$ T magnetic field ($L_\alpha \approx l_\alpha \ll l_B$). The magnetic length and the oscillator length start to become comparable only for magnetic fields ~ 100 T; below this field scale exciton states are weakly perturbed by magnetic fields.

Fig. 3 shows numerical results for the ground-state exciton energy at $B = 10$ T as a function of the lateral electron-hole separation s . When $s \gg L_e, L_h$, the electron and hole are confined in widely separated harmonic potentials, electron-hole correlations are negligible, and interactions can be treated at lowest order in perturbation theory. In this limit, the ground state energy is

$$E_{eh}^{(0)}(s) = E_e^{(0)} + E_h^{(0)} - \frac{e^2}{\epsilon \sqrt{s^2 + d^2}}, \quad (15)$$

where $E_e^{(0)} = \hbar(\Omega_{e+} + \Omega_{e-})/2 = \hbar\Omega_e$ is the ground state of an electron in the quantum dot (and similarly for holes) with Ω_{\pm} and Ω defined after Eq. (7). The dotted curves in Fig. 3 show that the approximate ground state energy calculated from Eq. (15), which entirely neglects electron-hole correlations, agrees well with the numerical results when $s \gg L_e, L_h$. For intermediate $s \sim 3$ nm, Coulomb attraction distorts the wavefunctions of the electron and hole, which effectively reduces the electron-hole separation and results in a lower ground-state energy than that given by the large- s approximation (15). For small s , the electron and hole wavefunctions overlap in the 2D plane and the approximation of Eq. (15), which becomes singular in this limit when $d = 0$, breaks down. The singular behavior at small s is cut off by the kinetic-energy pressure required by the Heisenberg uncertainty relation, and this results in a ground state energy that is higher than that given by Eq. (15). The approximate ground state energy of Eq. (15) is in reasonable agreement with numerical results when $s \gtrsim L_e, L_h$.

We see from Fig. 3 that exciton properties depend qualitatively on the ratio of s to confinement oscillator lengths. As indicated in Fig. 1, the experimentally relevant value of s is either $s = 0$, in which case electron-hole correlation is always important, or $s = a_M/\sqrt{3}$, where a_M is the lattice constant of the triangular moiré Bravais lattice. In the former case (see below) the large- s limit is never relevant. In the latter case, the large- s limit is always achieved at large enough moiré period since the oscillator length of electrons or holes in moiré materials varies [23, 37] approximately as the square root of the moiré period. The large- s limit is simple not only for excitons, but for any finite-particle-number electron-hole complex, since the interactions between electrons and holes V_{eh} (Eq. (6)) simply add an electrostatic contribution to energies and do not alter electronic wavefunctions.

If confinement is weak, the $s = 0$ system can be viewed as a tightly bound exciton of mass $M = m_e + m_h$ moving in a weak confining potential with angular frequency $\omega = \sqrt{(m_e\omega_e^2 + m_h\omega_h^2)/(m_e + m_h)}$ [64]. The ground state energy is then the sum of the ground state energies of the harmonic oscillator and the tightly bound exciton. For the intralayer exciton case $d = 0$, the system is similar to a 2D hydrogen atom, and the total energy is given by the analytic result:

$$E_{eh}^{(0)}(0) = \hbar\omega - 4\text{Ry}^*. \quad (16)$$

This approximate result is indicated by the blue cross in Fig. 3, where we see that the parameters chosen for this calculation are not in the weak confinement limit – the exciton radius $\sim a_B^*$ is not small compared with the confining length of the harmonic potential $L = \sqrt{\hbar/M\omega}$ – and Eq. (16) is therefore inaccurate. The stronger confinement weakens the correlations between electron and hole positions and therefore increases the total energy.

Fig. 4 shows how the exciton ground state energy shifts in a magnetic field. In the large- s limit it follows from

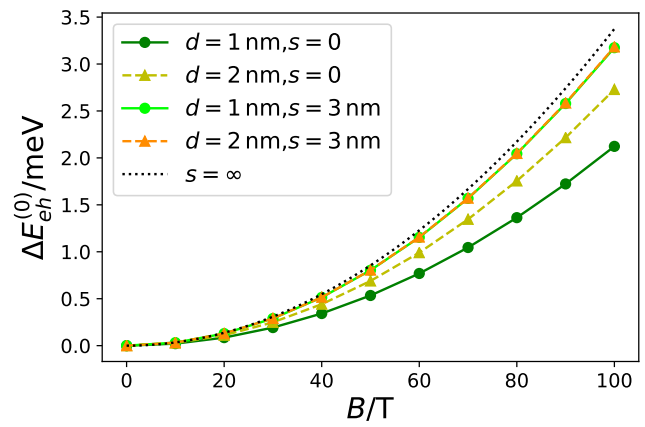


FIG. 4. Diamagnetic exciton energy shift $\Delta E_{eh}^{(0)}(B) = E_{eh}^{(0)}(B) - E_{eh}^{(0)}(B = 0)$ of the excitonic ground state in a magnetic field B , for interlayer excitons at $d = 1, 2$ nm and $s = 0, 3$ nm. The circular and triangular dots connected by solid or dashed lines are numerical results from ED calculations, and the dotted curve shows the energy increase obtained from the $s \rightarrow \infty$ limit (15) expression in which only the zero-point confinement energy is shifted.

Eq. (15) that the diamagnetic exciton energy shift comes from the single-particle energies of electrons and holes:

$$\begin{aligned} \Delta E_{eh}^{(0)}(B) &\equiv E_{eh}^{(0)}(B) - E_{eh}^{(0)}(B = 0) \\ &\xrightarrow{s \rightarrow \infty} \hbar(\Omega_e + \Omega_h - \omega_e - \omega_h) \\ &\approx \frac{e^2 B^2}{8} \left(\frac{l_e^2}{m_e} + \frac{l_h^2}{m_h} \right). \end{aligned} \quad (17)$$

The last line of the above equation applies for a small magnetic field $B \ll 2m_\alpha\omega_\alpha/e$. Fig. 4 shows that for $s = 3$ nm the numerical results are already close to the $s \rightarrow \infty$ limit. The diamagnetic exciton energy shift grows quadratically with magnetic field both in the strong-binding case ($s = 0$) and in the strong-confinement large- s limit, as expected for the ground state with zero angular momentum. By first-order perturbation theory we see from Eqs. (2) and (3) that the diamagnetic exciton energy shift for a zero-angular-momentum state is

$$\Delta E_{eh}^{(0)}(B) \approx \frac{e^2 B^2}{8} \left(\langle \mathbf{r}_e^2 \rangle + \langle \mathbf{r}_h^2 \rangle \right), \quad (18)$$

where the angle brackets denote ground state expectation values. When $s = 0$ the electron and hole orbitals shrink due to strong Coulomb attraction, resulting in a weaker diamagnetic response. The diamagnetic response of excitons can therefore be used as an experimental probe of the binding strength of the electrons and holes and therefore distinguish the case in which they localized at the same site from the case in which they are localized at different sites.

Next we study the optical absorption of the intralayer exciton states ($d = 0$). In our model the current operator

is given up to a constant factor by

$$\hat{j} \sim \sum_{\tau} \int d\mathbf{r} [e_{\tau}^{\dagger}(\mathbf{r}) h_{\tau}^{\dagger}(\mathbf{r}) \exp(i \frac{eBs}{2\hbar} y) + h_{\tau}(\mathbf{r}) e_{\tau}(\mathbf{r}) \exp(-i \frac{eBs}{2\hbar} y)], \quad (19)$$

where e^{\dagger} and h^{\dagger} are electron and hole creation operators, $\tau = \pm$ is the valley index, and the phase factors $\exp(\pm i \frac{eBs}{2\hbar} y)$ come from our gauge choice (see Appendix B for details). The matrix element for a transition from the vacuum state $|\Psi_0\rangle$ with no electrons or holes to an exciton state $|\Psi_{eh}^{(i)}\rangle$ (Eq. (14)) is proportional to

$$\langle \Psi_0 | \hat{j} | \Psi_{eh}^{(i)} \rangle \sim \sum_{n_e n_h} C_{n_e n_h}^{(i)} \int d\mathbf{r} \psi_{n_e}^{(e)}(\mathbf{r}) \psi_{n_h}^{(h)}(\mathbf{r}) e^{-i \frac{eBs}{2\hbar} y}, \quad (20)$$

where $\psi_{n_e}^{(e)}(\mathbf{r})$ is the wavefunction of an electron in state n_e , and similarly $\psi_{n_h}^{(h)}(\mathbf{r})$ for holes. Then the absorption rate of state i is proportional to the dimensionless quantity

$$A_{eh}^{(i)} = \left| \sum_{n_e n_h} C_{n_e n_h}^{(i)} \int d\mathbf{r} \psi_{n_e}^{(e)}(\mathbf{r}) \psi_{n_h}^{(h)}(\mathbf{r}) e^{-i \frac{eBs}{2\hbar} y} \right|^2, \quad (21)$$

which is, roughly speaking, the overlap of the electron and hole wavefunctions. The optical absorption strength of the ground state is calculated by numerical integration of the wavefunctions and shown in Fig. 5. The optical spectrum is a set of δ -function peaks located at the energy eigenvalues of exciton states and with heights proportional to the corresponding optical absorption rates:

$$A_{eh}(\omega) = \sum_i A_{eh}^{(i)} \delta(\hbar\omega - E_{eh}^{(i)} - E_g), \quad (22)$$

where E_g is the single-particle gap between the conduction and valence bands.

We can obtain analytic expressions for the optical matrix elements in certain limiting cases. When $s \gg L_e, L_h$ and confinement is strong the electron and hole are in the ground states of their confining potentials and their wavefunctions are

$$\psi_0^{(\alpha)}(\mathbf{r}) = \frac{1}{\sqrt{\pi}} \frac{1}{L_{\alpha}} e^{-r^2/2L_{\alpha}^2}, \quad (23)$$

where $\alpha = e, h$ and the origin $\mathbf{r} = 0$ is chosen at the bottom of the confining potential. The two-body wavefunction is approximately the product of $\psi_0^{(e)}$ and $\psi_0^{(h)}$. Then we can do the integral (21) and find

$$A_{eh}^{(0)}(s) \approx \left(\frac{2L_e L_h}{L_e^2 + L_h^2} \right)^2 \exp \left[-\frac{s^2}{L_e^2 + L_h^2} \left(1 + \frac{L_e^2 L_h^2}{4l_B^4} \right) \right]. \quad (24)$$

The dotted curve in Fig. 5 shows that the above approximation is in good agreement with the numerical results at large s .

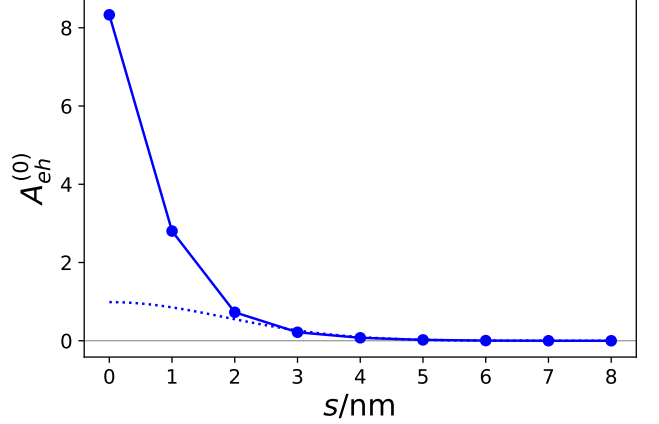


FIG. 5. Optical absorption strength $A_{eh}^{(0)}$ of intralayer excitons as a function of the separation between the electron and hole confining potential minima s . These results were calculated at magnetic field $B = 10$ T, but differ very little from results calculated at $B = 0$. The blue dots are the numerical results from ED calculations and the dotted curve is from the large- s approximation (24). Since the likely s is either 0 or $a_M/\sqrt{3}$, based on symmetry considerations, and typical moiré periods are longer than 5 nm, a substantial reduction in oscillator strength is expected in the $s \neq 0$ case.

For $s = 0$ and the weak-confinement limit, the wavefunction of the two-particle system can be separated into center-of-mass and relative motions

$$\Psi_{eh}^{(0)}(\mathbf{r}_e, \mathbf{r}_h) \approx \psi_{cm}(\mathbf{R}) \psi_{rel}(\mathbf{r}), \quad (25)$$

where $\mathbf{R} = (m_e \mathbf{r}_e + m_h \mathbf{r}_h)/M$ and $\mathbf{r} = \mathbf{r}_e - \mathbf{r}_h$ are the center-of-mass and relative coordinates. The center-of-mass motion is the ground state of the harmonic oscillator:

$$\psi_{cm}(\mathbf{R}) = \frac{1}{\sqrt{\pi}} \frac{1}{L} e^{-R^2/2L^2}, \quad (26)$$

where the confining length $L = \sqrt{\hbar/M\omega} = 1.30$ nm. The relative motion is the ground state of the 2D hydrogen atom

$$\psi_{rel}(\mathbf{r}) = \frac{1}{\sqrt{2\pi}} \frac{4}{a_B^*} e^{-2r/a_B^*}. \quad (27)$$

With the wavefunction (25) and the current operator (19) we find

$$\langle \Psi_0 | \hat{j} | \Psi_{eh}^{(0)} \rangle = \int d\mathbf{R} \Psi_{eh}^{(0)}(\mathbf{R}, \mathbf{R}) \approx 4\sqrt{2}L/a_B^*, \quad (28)$$

and therefore

$$A_{eh}^{(0)}(0) = |\langle \Psi_0 | \hat{j} | \Psi_{eh}^{(0)} \rangle|^2 \approx \frac{32L^2}{a_B^{*2}} \approx 38. \quad (29)$$

This estimate is much larger than the result from ED calculation, as shown in Fig. 5. The difference can be understood as follows. Confinement adds a harmonic repulsive contribution to the relative motion which mixes the

ground state of the 2D hydrogen atom (27) with higher energy states. Since the wavefunctions of higher-energy hydrogenic states have smaller values at $\mathbf{r} = 0$, the resulting optical absorption strength is reduced [65]. For the parameters used in the calculations illustrated in Fig. 5, the confining potential is far from weak, a lot of high energy states come into play, and the discrepancy between the exact numerical results and the approximation of (29) becomes large.

IV. TRIONS

Next we study a system of one electron and two holes – a moiré-confined trion. The three-particle state must be antisymmetric with respect to exchange of the two holes. We work in a representation in which the orbital and valley parts of the two-hole states separate, and each is symmetric or antisymmetric with respect to the permutation. The orbital parts of the basis states are ($n_{h1} > n_{h2}$)

$$|n_e; n_{h1}n_{h2}\rangle_s = \frac{1}{\sqrt{2}}|n_e\rangle_e(|n_{h1}n_{h2}\rangle_h + |n_{h2}n_{h1}\rangle_h), \quad (30)$$

$$|n_e; n_{h1}n_{h2}\rangle_a = \frac{1}{\sqrt{2}}|n_e\rangle_e(|n_{h1}n_{h2}\rangle_h - |n_{h2}n_{h1}\rangle_h), \quad (31)$$

$$|n_e; n_hn_h\rangle_s = |n_e\rangle_e|n_hn_h\rangle_h, \quad (32)$$

where each n is shorthand for the two indices (n_+, n_-) that distinguish two-dimensional oscillator single-particle states, the subscripts s and a stand for symmetric and antisymmetric states, and the kets with subscripts e and h are direct product states of electrons and holes without (anti)symmetrization. The valley parts of the basis states are

$$|\pm; ++\rangle_s = |\pm\rangle_e|++\rangle_h, \quad (33)$$

$$|\pm; --\rangle_s = |\pm\rangle_e|--\rangle_h, \quad (34)$$

$$|\pm; +- \rangle_s = \frac{1}{\sqrt{2}}|\pm\rangle_e(|+-\rangle_h + |-+\rangle_h), \quad (35)$$

$$|\pm; +- \rangle_a = \frac{1}{\sqrt{2}}|\pm\rangle_e(|+-\rangle_h - |-+\rangle_h), \quad (36)$$

where $+$ and $-$ stand for valley $+K$ and $-K$.

We are interested in the optical excitations of a state with a single hole to a trion one-electron-two-hole state. The initial hole is in the ground state $n_h = 0$ (by which we mean $n_{h+} = n_{h-} = 0$), and we assume without loss of generality that it is in the $-K$ valley:

$$|\Psi_h^{(0)}\rangle = |0\rangle_h|-\rangle_h. \quad (37)$$

In order for the optical matrix elements to be non-zero, the newly added electron and hole must be in the same valley. There are three possibilities: $|+; +- \rangle_a$, $|+; +- \rangle_s$ and $|--; -- \rangle_s$. Correspondingly the three-particle state has three possible forms:

$$|\Psi_{ehh}^{(1,i)}\rangle = \sum_{n_e} \sum_{n_{h1} \geq n_{h2}} C_{n_e n_{h1} n_{h2}}^{(s,i)} |n_e; n_{h1}n_{h2}\rangle_s |+; +- \rangle_a, \quad (38)$$

$$|\Psi_{ehh}^{(2,i)}\rangle = \sum_{n_e} \sum_{n_{h1} > n_{h2}} C_{n_e n_{h1} n_{h2}}^{(a,i)} |n_e; n_{h1}n_{h2}\rangle_a |+; +- \rangle_s, \quad (39)$$

$$|\Psi_{ehh}^{(3,i)}\rangle = \sum_{n_e} \sum_{n_{h1} > n_{h2}} C_{n_e n_{h1} n_{h2}}^{(a,i)} |n_e; n_{h1}n_{h2}\rangle_a |-; -- \rangle_s. \quad (40)$$

The energy of the system depends only on the orbital part of the state, so the second and third forms of the three-particle state (39) and (40) with antisymmetric orbital parts are exactly degenerate in energy. Exchange statistics suggests that the ground state takes the first

form (38), since there is then no exclusion principle that forbids the two holes from occupying the same low-energy single-particle orbital ($n_{h1} = n_{h2} = 0$). This expectation is confirmed by our numerical results.

Using the current operator (19), we find the optical absorption strength for intralayer trions

$$A_{ehh}^{(1,i)} = \left| \sum_{n_e} \int d\mathbf{r} \psi_{n_e}^{(e)}(\mathbf{r}) \left[\frac{1}{\sqrt{2}} \sum_{n_h > 0} C_{n_e n_h 0}^{(s,i)} \psi_{n_h}^{(h)}(\mathbf{r}) + C_{n_e 00}^{(s,i)} \psi_0^{(h)}(\mathbf{r}) \right] \exp(-i \frac{eBs}{2\hbar} y) \right|^2 \equiv A_{ehh}^{(s,i)}, \quad (41)$$

$$A_{ehh}^{(2,i)} = \frac{1}{2} \left| \sum_{n_e} \sum_{n_h > 0} C_{n_e n_h 0}^{(a,i)} \int d\mathbf{r} \psi_{n_e}^{(e)}(\mathbf{r}) \psi_{n_h}^{(h)}(\mathbf{r}) \exp(-i \frac{eBs}{2\hbar} y) \right|^2 \equiv A_{ehh}^{(a,i)}, \quad (42)$$

$$A_{ehh}^{(3,i)} = \left| \sum_{n_e} \sum_{n_h > 0} C_{n_e n_h 0}^{(a,i)} \int d\mathbf{r} \psi_{n_e}^{(e)}(\mathbf{r}) \psi_{n_h}^{(h)}(\mathbf{r}) \exp(-i \frac{eBs}{2\hbar} y) \right|^2 = 2A_{ehh}^{(a,i)}. \quad (43)$$

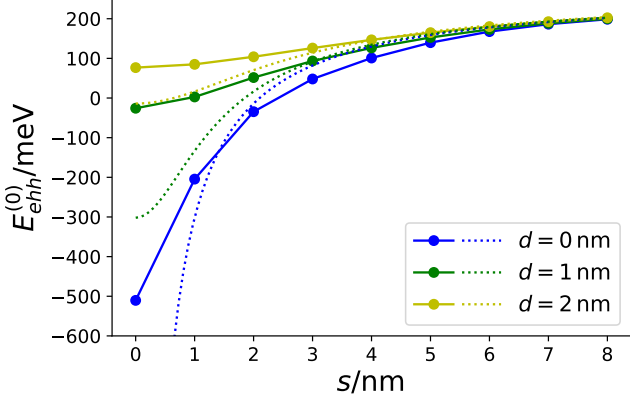


FIG. 6. Ground-state trion energy $E_{ehh}^{(0)}$ as a function of the separation between the electron and hole confining potential minima s , for intralayer ($d = 0$) and interlayer ($d = 1, 2$ nm) trions represented by different colors. The magnetic field $B = 10$ T. The dots and solid lines are numerical results from ED calculations, and the dotted curves show results from the large- s approximation (45).

When the polarization of the incident light is random (or equivalently, when the valley polarization of the initial hole is random), there is equal probability that an electron-hole pair is created in the same or opposite valley as the initial hole. Therefore the optical absorption spectrum is

$$\begin{aligned} A_{ehh}(\omega) &= \frac{1}{2} \sum_{p=1}^3 \sum_i A_{ehh}^{(p,i)} \delta(\hbar\omega - E_{ehh}^{(p,i)} - E_g) \\ &= \frac{1}{2} \sum_i A_{ehh}^{(s,i)} \delta(\hbar\omega - E_{eh}^{(s,i)} - E_g) \\ &\quad + \frac{3}{2} \sum_i A_{ehh}^{(a,i)} \delta(\hbar\omega - E_{ehh}^{(a,i)} - E_g). \end{aligned} \quad (44)$$

Fig. 6 shows the ground-state trion energy $E_{ehh}^{(0)}$ as a function of the electron-hole separation s . Other parameters of the calculations are chosen to be the same as for the calculations of excitons in Sec. III. The dotted curve shows the large- s approximation in which the motion of the electron (holes) is not affected by the presence of the holes (electron) in the other potential well, so the ground

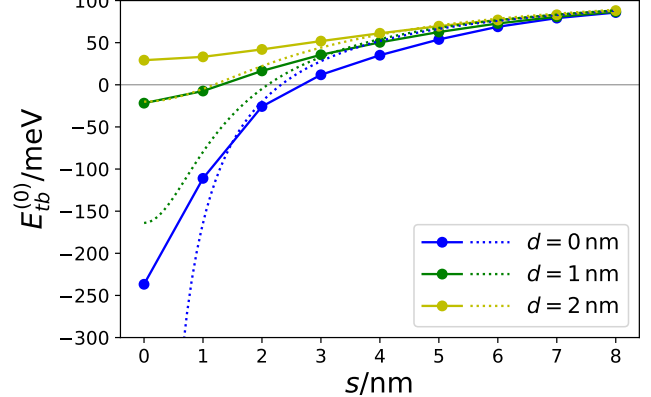


FIG. 7. Ground state trion binding energy E_{tb} as a function of the separation between the electron and hole confining potential minima s , for intralayer ($d = 0$) and interlayer ($d = 1, 2$ nm) trions represented by different colors. The magnetic field $B = 10$ T. The dots and solid lines are numerical results from ED calculations, and the dotted curves show results from the large- s approximation.

state energy is

$$E_{ehh}^{(0)}(s) \approx E_e^{(0)} + E_{hh}^{(0)} - \frac{2e^2}{\epsilon\sqrt{s^2 + d^2}}, \quad (45)$$

where $E_{hh}^{(0)}$ is the ground state energy of two holes in the same quantum dot. A similar ED calculation with only holes present yields $E_{hh}^{(0)} = 224$ meV for the parameters of Fig. 6. As shown in Fig. 6, the approximation (45) is in good agreement with the numerical results for $s \gtrsim L_e, L_h$.

Fig. 7 shows the trion binding energy, defined as

$$E_{tb} = E_{eh}^{(0)} + E_h^{(0)} - E_{ehh}^{(0)}, \quad (46)$$

as a function of s . At small s , an extra hole binds with the electron-hole pair in such a way as to lower the energy. At large s , the repulsion between the two holes dominates and the energy increases when an extra hole is added to the system. The crossover from a bound trion to an unbound trion takes place between 2 to 3 nm for an intralayer trion, and around 1 nm for an interlayer trion

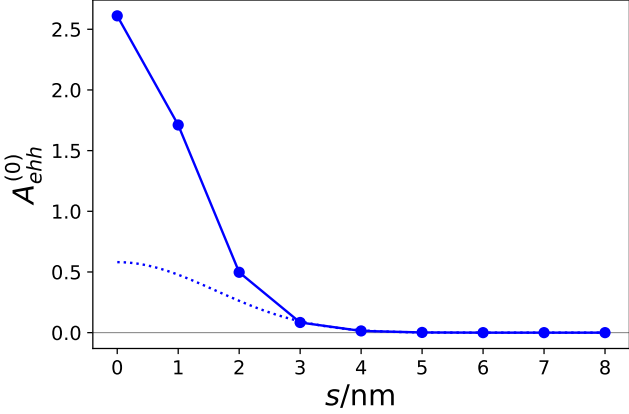


FIG. 8. Optical absorption strength $A_{ehh}^{(0)}$ of intralayer trions as a function of the separation between the electron and hole confining potential minima s . The magnetic field $B = 10$ T. The blue dots are numerical results from ED calculations, and the dotted curve is the large- s approximation (49).

at interlayer distance $d = 1$ nm. An interlayer trion at $d = 2$ nm is always unbound even for $s = 0$.

Fig. 8 shows the optical absorption strength $A_{ehh}^{(0)}$ as a function of s . Comparison with Fig. 5 shows that the optical absorption of an intralayer trion is always weaker

than that of an intralayer exciton. This can be qualitatively understood by considering the $m_e \rightarrow \infty$ limit at $s = 0$ for which the electron stays at the center of its quantum dot while the two holes move around it. The Coulomb repulsion between the two holes pushes them away from the electron into higher-energy states, so the overlap between the electron and hole wavefunctions, and therefore the optical absorption strength, decreases. For large $s \gg L_e, L_h$, the optical absorption strength is small and can be calculated from Eq. (41) with

$$C_{n_e n_{h1} n_{h2}}^{(s,0)} = \delta_{n_e,0} C_{n_{h1} n_{h2}}^{(s,0)}, \quad (47)$$

where $C_{n_{h1} n_{h2}}^{(s,0)}$ (with $n_{h1} > n_{h2}$) are the expansion coefficients of the two-hole ground state in the symmetric two-hole basis. We notice from the ED calculation that the two-hole ground state comes predominantly from the single-particle ground state $|00,00\rangle_s$ and the lowest two excited states with zero total angular momentum $|11,00\rangle_s$ and $|10,01\rangle_s$:

$$|\Psi_{hh}^{(0)}\rangle \approx C_0|00,00\rangle_s + C_1|11,00\rangle_s + C_2|10,01\rangle_s, \quad (48)$$

with $C_0 \approx 0.80$ and $C_1 \approx C_2 \approx 0.42$. Then from Eq. (41) we find an analytic expression for the optical absorption strength in the large- s limit:

$$A_{ehh}^{(0)}(s) \approx \left| C_0 - \frac{C_1}{\sqrt{2}} \left[\frac{L_e^2 - L_h^2}{L_e^2 + L_h^2} + \left(1 - \frac{L_e^4}{4l_B^4}\right) \frac{L_h^2 s^2}{L_e^2 + L_h^2} \right] \right|^2 \left(\frac{2L_e L_h}{L_e^2 + L_h^2} \right)^2 \exp \left[-\frac{s^2}{L_e^2 + L_h^2} \left(1 + \frac{L_e^2 L_h^2}{4l_B^4} \right) \right]. \quad (49)$$

This approximation is in good agreement with the numerical results at $s \gtrsim 3$ nm as shown by the dotted curve in Fig. 8.

V. SUMMARY AND DISCUSSION

In this article we have numerically calculated the energies of exciton and trion states in moiré superlattices, and the matrix elements for interband absorption processes with exciton and trion final states. We have modeled the moiré superlattice by harmonic confinement potentials – an approximation that is valid when the confinement oscillator lengths are small compared to the moiré lattice constant. Our calculations are similar to earlier ones [63–66] that used harmonic confinement potentials to model quantum dots in semiconductor quantum wells, but differ because of the relevance of the TMD valley degree of freedom, and by the possibility in the moiré superlattice case that electrons and holes are localized at different lattice sites.

The relative positions of electron and hole confinement locations is very important for the optical properties of

moiré superlattices. As illustrated in Fig. 1, the two most likely possibilities are that the confinement locations are at identical positions in the moiré unit cell, or that they are separated by a large fraction of the moiré lattice constant. It is not yet known whether one circumstance or the other is always realized, or whether this important distinction is interface-dependent. Our calculations show that the two cases should be easily observable experimentally, since the rotational symmetries that apply approximately in the common-confinement-location case, lead to a small number of very strong absorption peaks. In the distinct-confinement-location case, the number of exciton and trion absorption peaks proliferates as angular-momentum-conservation selection rules are relaxed, but the overall absorption strength is still weakened due to electron-hole confinement. Because the Bohr radius length scale is so short in TMD two-dimensional semiconductors, the influence of magnetic fields on observable properties is weak at moderate magnetic field strengths. In fact most of our illustrative calculations were carried out at a magnetic field $B = 10$ T, but are nearly identical to the results we obtain at $B = 0$. Magnetic fields are potentially very useful probes in sort-

ing out the properties of electron-hole systems formed at particular interfaces, but will require extremely strong magnetic fields on the 100 T scale.

A full theory of the optical absorption spectrum of a doped moiré system is complicated by importance of correlations among the doped charges present in the initial state and correlations between electrons, holes, and trions located in different periods of the moiré superlattice [52]. As a first approximation, we ignore these complications and assume that at filling factor $\nu \in (0, 1)$, the optical spectrum is simply a weighted average of the exciton and trion spectra:

$$A_\nu(\omega) = (1 - \nu)A_{eh}(\omega) + \nu A_{ehh}(\omega). \quad (50)$$

with A_{eh} and A_{ehh} given by Eqs. (22) and (44). The numerical results are shown in Fig. 9, for a large $s = 3 \text{ nm}$ (a) and a small $s = 1 \text{ nm}$ (b). The magnetic field $B = 10 \text{ T}$, and all other parameters are the same as in Secs. III and IV. The band gap E_g is set to zero in this figure since its only effect is a constant shift along the ω -axis. The δ -function is replaced with a Lorentzian function with height 1 and width 0.2 meV. At $s = 1 \text{ nm}$ the electrons and holes are strongly bound and the two- or three-body eigenstates of the system have approximate rotational symmetry, so most of these states have optical absorption that is suppressed by angular momentum conservation [49, 63]. In contrast, at $s = 3 \text{ nm}$ the electrons and holes are strongly localized in the harmonic potentials, and Coulomb interaction distorts the localized wavefunctions weakly. In this case the selection rules associated with angular momentum conservation are not relevant because rotational symmetry is strongly broken. The absorption peaks in Fig. 9(a) are therefore much more closely spaced than in Fig. 9(b). The peaks for states with nonzero angular momenta appear in the strong-confinement limit and are split in a magnetic field (e.g., the exciton peaks near 40 meV in Fig. 9(a)). The results do demonstrate that the absorption spectrum of moiré superlattices is strongly sensitive to electrical modulation of the carrier density.

A more accurate description of the optical spectra of moiré materials would take account of correlations between electrons and holes in different periods of the moiré pattern, but is beyond the scope of the present work. These correlations will entangle photons emitted by nearby excitons, and promise the possibility of realizing unusual single and few photon light emitters. Intervalley exchange interactions are crucial for the topological properties of point-particle-like moiré excitons [38] and are expected to play an important role for our case of spatially distorted excitons and trions as well. Our work has focused on excitons and trions, but our method also applies to more complex systems like biexcitons. Because the moiré confinement length is relatively small, the trans-

sition energy between excitons and biexcitons localized at a single moiré site is expected to be large. The method can also be extended to study a combination of localized and itinerant particles, which may help interpret recent

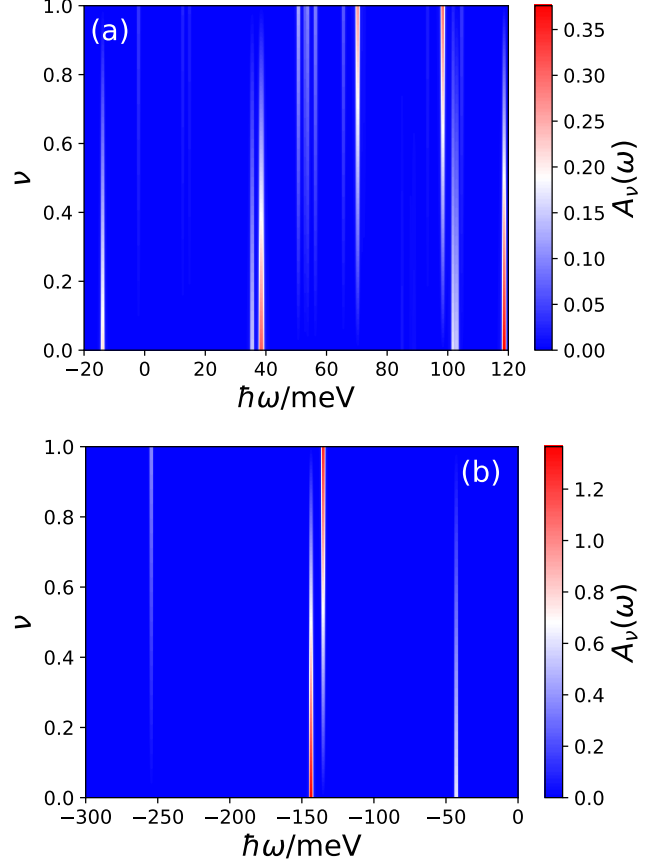


FIG. 9. The optical absorption spectra as the ground state hole moiré filling factor ν varies from 0 to 1, assuming that excitons, holes, and trions centered on different sites are not correlated. These results were calculated at (a) $s = 3 \text{ nm}$; (b) $s = 1 \text{ nm}$.

experimental work [26, 72] that used excitons in a TMD monolayer as an optical sensor of correlated insulating states in moiré materials. We anticipate that close interaction between theory and experiment will be necessary to sort out all the richness of the optical properties of moiré superlattices.

ACKNOWLEDGMENTS

Y.Z. and A.H.M. acknowledge many helpful conversations with Hui Deng and Feng Wang. This work was supported by Army Research Office (ARO) Grant # W911NF-17-1-0312 (MURI).

Appendix A: Derivation of Coulomb matrix elements in the harmonic oscillator basis

1. Single-particle basis

We consider an electron or a hole moving in a two-dimensional quantum dot, described by the Hamiltonian

$$H = \frac{1}{2m}(\mathbf{p} \pm e\mathbf{A}) + \frac{1}{2}m\omega^2\mathbf{r}^2, \quad (\text{A1})$$

where the upper and lower signs are for electrons and holes respectively. We work in the symmetric gauge

$$A_x = -By/2, \quad A_y = Bx/2. \quad (\text{A2})$$

To simplify notations we define the dimensionless quantities

$$\tilde{\mathbf{r}} = \mathbf{r}/l_B, \quad \tilde{\omega} = \omega/\omega_c, \quad \tilde{H} = H/\hbar\omega_c, \quad (\text{A3})$$

where the magnetic length $l_B = \sqrt{\hbar/eB}$ and the cyclotron frequency $\omega_c = eB/m$. The dimensionless Hamiltonian can then be written as

$$\tilde{H} = \frac{1}{2}(-i\partial_{\tilde{x}} \mp \frac{\tilde{y}}{2})^2 + \frac{1}{2}(-i\partial_{\tilde{y}} \pm \frac{\tilde{x}}{2}) + \frac{1}{2}\tilde{\omega}^2(\tilde{x}^2 + \tilde{y}^2). \quad (\text{A4})$$

Now we transform to the complex coordinates

$$z = x + iy, \quad z^* = x - iy, \quad (\text{A5})$$

and their dimensionless counterparts \tilde{z}, \tilde{z}^* defined in an obvious way. Then after some algebra the Hamiltonian can be written as

$$\tilde{H} = -2\partial_{\tilde{z}^*}\partial_{\tilde{z}} + (\frac{1}{8} + \frac{1}{2}\tilde{\omega}^2)\tilde{z}^*\tilde{z} \pm \frac{1}{2}(\tilde{z}\partial_{\tilde{z}} - \tilde{z}^*\partial_{\tilde{z}^*}). \quad (\text{A6})$$

Now we introduce the operators

$$\begin{aligned} b_+ &= \frac{1}{\sqrt{2}}(\frac{\tilde{z}^*}{2} + 2\partial_{\tilde{z}}), & b_+^\dagger &= \frac{1}{\sqrt{2}}(\frac{\tilde{z}}{2} - 2\partial_{\tilde{z}^*}), \\ b_- &= \frac{1}{\sqrt{2}}(\frac{\tilde{z}}{2} + 2\partial_{\tilde{z}^*}), & b_-^\dagger &= \frac{1}{\sqrt{2}}(\frac{\tilde{z}^*}{2} - 2\partial_{\tilde{z}}), \end{aligned} \quad (\text{A7})$$

which satisfy the usual commutation relations of raising and lowering ladder operators. The Hamiltonian can be written in terms of these operators as

$$\tilde{H} = b_\pm^\dagger b_\pm + \frac{1}{2} + \tilde{\omega}^2(b_+^\dagger + b_-)(b_+ + b_-^\dagger), \quad (\text{A8})$$

where as before the upper and lower signs (in the subscript) are for electrons and holes respectively. The Hamiltonian is quadratic in the ladder operators, and can be diagonalized by a Bogoliubov transformation

$$\begin{aligned} a_+ &= b_\pm \cosh \frac{\eta}{2} + b_\mp^\dagger \sinh \frac{\eta}{2}, \\ a_- &= b_\mp \cosh \frac{\eta}{2} + b_\pm^\dagger \sinh \frac{\eta}{2}, \end{aligned} \quad (\text{A9})$$

where

$$\tanh \eta = \frac{2\tilde{\omega}^2}{2\tilde{\omega}^2 + 1} = \frac{2\omega^2}{2\omega^2 + \omega_c^2}. \quad (\text{A10})$$

The Hamiltonian then takes the diagonal form

$$\tilde{H} = \tilde{\Omega}_+(a_+^\dagger a_+ + \frac{1}{2}) + \tilde{\Omega}_-(a_-^\dagger a_- + \frac{1}{2}), \quad (\text{A11})$$

where

$$\tilde{\Omega}_{\pm} = \frac{1}{2}(\sqrt{1 + 4\tilde{\omega}^2} \pm 1). \quad (\text{A12})$$

Restoring the physical dimensions, we have the diagonalized Hamiltonian

$$H = \hbar\Omega_+(a_+^\dagger a_+ + \frac{1}{2}) + \hbar\Omega_-(a_-^\dagger a_- + \frac{1}{2}), \quad (\text{A13})$$

with

$$\Omega_{\pm} = \sqrt{\omega^2 + (\frac{\omega_c}{2})^2} \pm \frac{\omega_c}{2} \equiv \Omega \pm \frac{\omega_c}{2}. \quad (\text{A14})$$

The eigenstates of this Hamiltonian are

$$|n_+ n_-\rangle = (a_+^\dagger)^{n_+} (a_-^\dagger)^{n_-} |0\rangle, \quad (\text{A15})$$

with energy

$$E_{n_+ n_-} = (n_+ + \frac{1}{2})\hbar\Omega_+ + (n_- + \frac{1}{2})\hbar\Omega_-. \quad (\text{A16})$$

For later use, the complex coordinate z can be expressed in terms of the ladder operators as

$$z = \sqrt{2}l_B(b_+^\dagger + b_-) = \sqrt{2}l_B e^{-\eta/2}(a_\pm^\dagger + a_\mp) = L(a_\pm^\dagger + a_\mp), \quad (\text{A17})$$

where $L = \sqrt{2}l_B e^{-\eta/2} = \sqrt{\hbar/m\Omega}$ is the total confining length. The normalized real-space wavefunction of the energy eigenstates is

$$\psi_{n_+ n_-}(r, \theta) = \left[\frac{n!}{(n + |l|)!} \frac{1}{\pi} \frac{1}{L} \right]^{1/2} \left(\frac{r}{L} \right)^{|l|} e^{-r^2/2L^2} L_n^{|l|}(r^2/L^2) \cdot e^{il\theta}, \quad (\text{A18})$$

where $n = \min(n_+, n_-)$, $l = \pm(n_+ - n_-)$, $\Omega = \sqrt{\omega^2 + (\omega_c/2)^2}$, and $L_n^{|l|}$ is the associated Laguerre polynomial.

2. Coulomb matrix elements

Now we calculate the Coulomb matrix elements in the above basis (generalized to multiple particles, see Eq. (8)). We start with the most complicated one, V_{eh} (Eq. (6)), the electron-hole interaction. The calculations for V_{ee} and V_{hh} are similar and simpler. We first write V_{eh} in Fourier form (consider only one electron and one hole for simplicity):

$$V_{eh} = -\frac{2\pi e^2}{\epsilon} \int \frac{d^2q}{(2\pi)^2} \frac{1}{|q|} e^{-|q|d} e^{iq_x s} e^{i(q^* z_e + q z_e^*)/2} e^{-i(q^* z_h + q z_h^*)/2}, \quad (\text{A19})$$

where $q = q_x + iq_y$ is a complex integration variable. By Eq. (A17) we can write the complex coordinates z in terms of ladder operators a_{\pm}, a_{\pm}^\dagger , then the matrix elements of V_{eh} can be written as

$$\begin{aligned} \langle n'_{e+} n'_{e-}, n'_{h+} n'_{h-} | V_{eh} | n_{e+} n_{e-}, n_{h+} n_{h-} \rangle &= -\frac{2\pi e^2}{\epsilon} \int \frac{d^2q}{(2\pi)^2} \frac{1}{|q|} e^{-|q|d} e^{iq_x s} \langle n'_{e+} | e^{iL_e(q^* a_{e+}^\dagger + q a_{e+})} | n_{e+} \rangle \\ &\times \langle n'_{e-} | e^{iL_e(q^* a_{e-}^\dagger + q a_{e-})} | n_{e-} \rangle \langle n'_{h+} | e^{-iL_h(q a_{h+}^\dagger + q^* a_{h+})} | n_{h+} \rangle \langle n'_{h-} | e^{-iL_h(q a_{h-}^\dagger + q^* a_{h-})} | n_{h-} \rangle, \end{aligned} \quad (\text{A20})$$

Then we need to evaluate matrix elements of the form $\langle n' | e^{i(f a^\dagger + f^* a)} | n \rangle$. To this end we make use of the operator identity

$$e^{i(f a^\dagger + f^* a)} = e^{-|f|^2/2} e^{i f a^\dagger} e^{i f^* a}, \quad (\text{A21})$$

which then leads to

$$\begin{aligned}
\langle n' | e^{i(fa^\dagger + f^* a)} | n \rangle &= e^{-|f|^2/2} \langle n' | e^{ifa^\dagger} e^{if^* a} | n \rangle \\
&= e^{-|f|^2/2} \sum_{k'=0}^{n'} \sum_{k=0}^n \frac{(if)^{k'} (if^*)^k}{k'! k!} \langle n' | (a^\dagger)^{k'} a^k | n \rangle \\
&= e^{-|f|^2/2} (ie^{i\varphi})^{n'-n} (n'! n!)^{1/2} \sum_{k=0}^{\min(n', n)} \frac{(-1)^{n-k} |f|^{n'+n-2k}}{k! (n'-k)! (n-k)!},
\end{aligned} \tag{A22}$$

where φ is the argument of the complex number $f = |f|e^{i\varphi}$. With this formula we go back to Eq. (A20) and get

$$\begin{aligned}
\langle n'_{e+} n'_{e-}, n'_{h+} n'_{h-} | V_{eh} | n_{e+} n_{e-}, n_{h+} n_{h-} \rangle &= -\sqrt{\frac{\beta_{eh}}{2}} \frac{e^2}{\epsilon l_B} \left(\prod_{\alpha\lambda} n'_{\alpha\lambda}! n_{\alpha\lambda}! \right)^{1/2} (-1)^{n'_{e+} + n_{e-} + n'_{h+} + n_{h-}} \\
&\times \sum_{k_{\alpha\lambda}=0}^{\min(n'_{\alpha\lambda}, n_{\alpha\lambda})} \left(\prod_{\alpha\lambda} \frac{(-1)^{k_{\alpha\lambda}} (\frac{\beta_{eh}}{\beta_\alpha})^{\frac{1}{2}(n'_{\alpha\lambda} + n_{\alpha\lambda}) - k_{\alpha\lambda}}}{k_{\alpha\lambda}! (n'_{\alpha\lambda} - k_{\alpha\lambda})! (n_{\alpha\lambda} - k_{\alpha\lambda})!} \right) \cdot I,
\end{aligned} \tag{A23}$$

where the summation indices $\alpha = e, h$ and $\lambda = \pm$ (the summation sign really means four summations), and we defined $\beta_\alpha = e^{\eta_\alpha} = \sqrt{1 + (2\omega_\alpha/\omega_{\alpha c})^2}$ and $\beta_{eh} = (\beta_e^{-1} + \beta_h^{-1})^{-1}$, and the (n', n, k) -dependent integral

$$I = \int_0^\infty d\tilde{q}^2 e^{-\tilde{q}^2} (\tilde{q}^2)^{p-\frac{1}{2}} e^{-\tilde{q}d} \cdot \int_0^{2\pi} \frac{d\phi}{2\pi} (ie^{i\phi})^{l-l'} e^{i\tilde{q}\tilde{s} \cos \phi}, \tag{A24}$$

with the dimensionless variables

$$\tilde{q} = \frac{l_B}{\sqrt{2\beta_{eh}}} |q|, \quad \tilde{d} = \frac{\sqrt{2\beta_{eh}}}{l_B} d, \quad \tilde{s} = \frac{\sqrt{2\beta_{eh}}}{l_B} s, \tag{A25}$$

the index

$$p = \sum_{\alpha\lambda} \left(\frac{n'_{\alpha\lambda} + n_{\alpha\lambda}}{2} - k_{\alpha\lambda} \right) \tag{A26}$$

and the total angular momentum quantum numbers

$$l = n_{e+} - n_{e-} - n_{h+} + n_{h-}, \quad l' = n'_{e+} - n'_{e-} - n'_{h+} + n'_{h-}. \tag{A27}$$

The integral (A24) can be simplified in special cases. When $s = 0$, the angular integral is simply $\delta_{l'l}$. When d is also zero, the radial integral yields a gamma function and the result is

$$I = \delta_{l'l} \cdot \Gamma(p + \frac{1}{2}). \tag{A28}$$

When $s = 0$ and $d \neq 0$, the radial integral yields the product of a gamma function and a (Tricomi's) confluent hypergeometric function

$$I = \delta_{l'l} \cdot 4^{-p} \Gamma(2p + 1) U(p + \frac{1}{2}, \frac{1}{2}, \frac{\tilde{d}^2}{4}). \tag{A29}$$

However, in the general case where $s \neq 0$, only the radial part can be integrated in closed form and the angular integral remains:

$$I = 4^{-p} \Gamma(2p + 1) \int_0^{2\pi} \frac{d\phi}{2\pi} (ie^{i\phi})^{l-l'} U(p + \frac{1}{2}, \frac{1}{2}, \frac{1}{4}(\tilde{d} - i\tilde{s} \cos \phi)^2). \tag{A30}$$

In practical calculations the integral has to be done numerically. The matrix elements of V_{ee} and V_{hh} can be calculated in the same way, although the result looks simpler since $d = s = 0$ for the same type of particles. The result is (without

antisymmetrization)

$$\begin{aligned} \langle n'_{1+} n'_{1-}, n'_{2+} n'_{2-} | V_{\alpha\alpha} | n_{1+} n_{1-}, n_{2+} n_{2-} \rangle &= \frac{\sqrt{\beta_\alpha}}{2} \frac{e^2}{\epsilon l_B} \left(\prod_{i\lambda} n'_{i\lambda}! n_{i\lambda}! \right)^{1/2} (-1)^{n'_{1+} + n_{1-} + n'_{2+} + n_{2-}} \delta_{l'l} \\ &\times \sum_{k_{i\lambda}=0}^{\min(n'_{i\lambda}, n_{i\lambda})} \left(\prod_{i\lambda} \frac{(-1)^{k_{i\lambda}} 2^{-p}}{k_{i\lambda}! (n'_{i\lambda} - k_{i\lambda})! (n_{i\lambda} - k_{i\lambda})!} \right) \cdot \Gamma(p + \frac{1}{2}), \end{aligned} \quad (\text{A31})$$

where $\alpha = e$ or h , the summation indices $i = 1, 2$ is the particle label (the e/h label is omitted), $\lambda = \pm$, and we defined

$$p = \sum_{i\lambda} \left(\frac{n'_{i\lambda} + n_{i\lambda}}{2} - k_{i\lambda} \right), \quad (\text{A32})$$

$$l = n_{1+} - n_{1-} + n_{2+} - n_{2-}, \quad l' = n'_{1+} - n'_{1-} + n'_{2+} - n'_{2-}. \quad (\text{A33})$$

Appendix B: The current operator

In the two-band model the current operator is (naively) proportional to $\sum_{\mathbf{k}} (e_{\mathbf{k}}^\dagger h_{-\mathbf{k}}^\dagger + h_{-\mathbf{k}} e_{\mathbf{k}})$, which in real space takes the form

$$\hat{j} \sim \int d\mathbf{r} [e^\dagger(\mathbf{r}) h^\dagger(\mathbf{r}) + h(\mathbf{r}) e(\mathbf{r})], \quad (\text{B1})$$

where e and h are annihilation operators of electron and hole states. Note however that in writing Eqs. (2) and (3) with $\mathbf{A}_\alpha(\mathbf{r}_\alpha) = \frac{1}{2} \mathbf{B} \times \mathbf{r}_\alpha$ for both $\alpha = e$ and h , and with \mathbf{r}_e and \mathbf{r}_h measured from different origins (see Fig. 2), we have implicitly performed a gauge transformation

$$\mathbf{A}_e(\mathbf{r}_e) \rightarrow \mathbf{A}_e(\mathbf{r}_e) - \frac{Bs}{2} \hat{y}, \quad \psi(\{\mathbf{r}_{ei}\}, \{\mathbf{r}_{hj}\}) \rightarrow \psi(\{\mathbf{r}_{ei}\}, \{\mathbf{r}_{hj}\}) \exp \left(i \frac{eBs}{2\hbar} \sum_i y_{ei} \right), \quad (\text{B2})$$

compared to the gauge where $\mathbf{A}(\mathbf{r}) = \frac{1}{2} \mathbf{B} \times \mathbf{r}$ for both electrons and holes, with the origin set at the confining potential minimum for holes. After the gauge transformation the field operator $e(\mathbf{r})$ gains an \mathbf{r} -dependent phase factor, so in this gauge the current operator becomes

$$\hat{j} \sim \int d\mathbf{r} \left[e^\dagger(\mathbf{r}) h^\dagger(\mathbf{r}) \exp \left(i \frac{eBs}{2\hbar} y \right) + h(\mathbf{r}) e(\mathbf{r}) \exp \left(-i \frac{eBs}{2\hbar} y \right) \right]. \quad (\text{B3})$$

Appendix C: Basis cutoff

s/nm	0	1	2	3	4	5	6	7	8
N_{x0}	150000	3000	3000	2000	2000	500	200	100	100
N_{t0}	500000	10000	8000	8000	8000	4000	4000	4000	4000
N_{x1}	20000	2000	1000	500	200	100	100	100	100
N_{t1}	50000	10000	5000	5000	4000	4000	4000	4000	4000
N_{x2}	10000	2000	1000	500	200	100	100	100	100
N_{t2}	20000	4000	4000	4000	4000	4000	4000	4000	4000

TABLE I. Number of basis states for the ED calculations for excitons (N_{x0}, N_{x1}, N_{x2} for $d = 0, 1, 2$ nm) and trions (N_{t0}, N_{t1}, N_{t2}) at different in-plane electron-hole separations s .

The energies and optical absorption strengths are obtained by numerically diagonalizing the Hamiltonian (1) as a matrix in the harmonic oscillator basis, which has to be cut off under some energy scale. The number of basis states used in the ED calculations are shown in Table I. With the exception of the $s = 0$ case, the number of basis states

is chosen such that the ground-state energy is accurate within 1 meV (in fact the error is much smaller for large s), and the optical absorption strength (for $d = 0$) is accurate within 1%. In the magnetic harmonic oscillator basis, convergence is faster for larger s . For $s = 0$, the ED calculations suffer from poor convergence with the number of basis states, as already noted in Ref. [64] where the exciton problem is solved instead in the center-of-mass and relative coordinates. However, since we are mostly interested in the $s \neq 0$ case, and for its easier generalization to more complicated systems like trions and biexcitons, we solve the $s = 0$ case also in the harmonic oscillator basis, but with a huge number of basis states. The calculation is manageable when we take advantage of the rotational symmetry of the system and only diagonalize the block with total angular momentum zero (which contains the ground state and is optically active).

[1] R. Bistritzer and A. H. MacDonald, Moiré bands in twisted double-layer graphene, *Proceedings of the National Academy of Sciences* **108**, 12233 (2011).

[2] Y. Cao, V. Fatemi, A. Demir, S. Fang, S. L. Tomarken, J. Y. Luo, J. D. Sanchez-Yamagishi, K. Watanabe, T. Taniguchi, E. Kaxiras, *et al.*, Correlated insulator behaviour at half-filling in magic-angle graphene superlattices, *Nature* **556**, 80 (2018).

[3] Y. Cao, V. Fatemi, S. Fang, K. Watanabe, T. Taniguchi, E. Kaxiras, and P. Jarillo-Herrero, Unconventional superconductivity in magic-angle graphene superlattices, *Nature* **556**, 43 (2018).

[4] X. Lu, P. Stepanov, W. Yang, M. Xie, M. A. Aamir, I. Das, C. Urgell, K. Watanabe, T. Taniguchi, G. Zhang, *et al.*, Superconductors, orbital magnets and correlated states in magic-angle bilayer graphene, *Nature* **574**, 653 (2019).

[5] M. Yankowitz, S. Chen, H. Polshyn, Y. Zhang, K. Watanabe, T. Taniguchi, D. Graf, A. F. Young, and C. R. Dean, Tuning superconductivity in twisted bilayer graphene, *Science* **363**, 1059 (2019).

[6] H. C. Po, L. Zou, A. Vishwanath, and T. Senthil, Origin of mott insulating behavior and superconductivity in twisted bilayer graphene, *Physical Review X* **8**, 031089 (2018).

[7] M. Koshino, N. F. Yuan, T. Koretsune, M. Ochi, K. Kuroki, and L. Fu, Maximally localized Wannier orbitals and the extended Hubbard model for twisted bilayer graphene, *Physical Review X* **8**, 031087 (2018).

[8] A. Kerelsky, L. J. McGilly, D. M. Kennes, L. Xian, M. Yankowitz, S. Chen, K. Watanabe, T. Taniguchi, J. Hone, C. Dean, *et al.*, Maximized electron interactions at the magic angle in twisted bilayer graphene, *Nature* **572**, 95 (2019).

[9] M. Serlin, C. Tschirhart, H. Polshyn, Y. Zhang, J. Zhu, K. Watanabe, T. Taniguchi, L. Balents, and A. Young, Intrinsic quantized anomalous hall effect in a moiré heterostructure, *Science* **367**, 900 (2020).

[10] J. Kang and O. Vafek, Symmetry, maximally localized Wannier states, and a low-energy model for twisted bilayer graphene narrow bands, *Physical Review X* **8**, 031088 (2018).

[11] H. Isobe, N. F. Yuan, and L. Fu, Unconventional superconductivity and density waves in twisted bilayer graphene, *Physical Review X* **8**, 041041 (2018).

[12] F. Wu, A. MacDonald, and I. Martin, Theory of phonon-mediated superconductivity in twisted bilayer graphene, *Physical review letters* **121**, 257001 (2018).

[13] B. Lian, Z. Wang, and B. A. Bernevig, Twisted bilayer graphene: a phonon-driven superconductor, *Physical review letters* **122**, 257002 (2019).

[14] M. Xie and A. H. MacDonald, Nature of the correlated insulator states in twisted bilayer graphene, *Physical review letters* **124**, 097601 (2020).

[15] Y. Cao, D. Rodan-Legrain, O. Rubies-Bigorda, J. M. Park, K. Watanabe, T. Taniguchi, and P. Jarillo-Herrero, Tunable correlated states and spin-polarized phases in twisted bilayer-bilayer graphene, *Nature* **583**, 215 (2020).

[16] E. Y. Andrei and A. H. MacDonald, Graphene bilayers with a twist, *Nature Materials* **19**, 1265 (2020).

[17] L. Balents, C. R. Dean, D. K. Efetov, and A. F. Young, Superconductivity and strong correlations in moiré flat bands, *Nature Physics* **16**, 725 (2020).

[18] U. Zondiner, A. Rozen, D. Rodan-Legrain, Y. Cao, R. Queiroz, T. Taniguchi, K. Watanabe, Y. Oreg, F. von Oppen, A. Stern, *et al.*, Cascade of phase transitions and dirac revivals in magic-angle graphene, *Nature* **582**, 203 (2020).

[19] D. Wong, K. P. Nuckolls, M. Oh, B. Lian, Y. Xie, S. Jeon, K. Watanabe, T. Taniguchi, B. A. Bernevig, and A. Yazdani, Cascade of electronic transitions in magic-angle twisted bilayer graphene, *Nature* **582**, 198 (2020).

[20] N. Bultinck, E. Khalaf, S. Liu, S. Chatterjee, A. Vishwanath, and M. P. Zaletel, Ground state and hidden symmetry of magic-angle graphene at even integer filling, *Physical Review X* **10**, 031034 (2020).

[21] J. M. Park, Y. Cao, K. Watanabe, T. Taniguchi, and P. Jarillo-Herrero, Tunable strongly coupled superconductivity in magic-angle twisted trilayer graphene, *Nature* **590**, 249 (2021).

[22] E. Khalaf, S. Chatterjee, N. Bultinck, M. P. Zaletel, and A. Vishwanath, Charged skyrmions and topological origin of superconductivity in magic-angle graphene, *Science advances* **7**, eabf5299 (2021).

[23] F. Wu, T. Lovorn, E. Tutuc, and A. H. MacDonald, Hubbard model physics in transition metal dichalcogenide moiré bands, *Physical review letters* **121**, 026402 (2018).

[24] E. C. Regan, D. Wang, C. Jin, M. I. B. Utama, B. Gao, X. Wei, S. Zhao, W. Zhao, Z. Zhang, K. Yumigeta, *et al.*, Mott and generalized Wigner crystal states in WSe₂/WS₂ moiré superlattices, *Nature* **579**, 359 (2020).

[25] Y. Tang, L. Li, T. Li, Y. Xu, S. Liu, K. Barakat, K. Watanabe, T. Taniguchi, A. H. MacDonald,

J. Shan, *et al.*, Simulation of hubbard model physics in WSe₂/WS₂ moiré superlattices, *Nature* **579**, 353 (2020).

[26] Y. Xu, S. Liu, D. A. Rhodes, K. Watanabe, T. Taniguchi, J. Hone, V. Elser, K. F. Mak, and J. Shan, Correlated insulating states at fractional fillings of moiré superlattices, *Nature* **587**, 214 (2020).

[27] L. Wang, E.-M. Shih, A. Ghiotto, L. Xian, D. A. Rhodes, C. Tan, M. Claassen, D. M. Kennes, Y. Bai, B. Kim, *et al.*, Correlated electronic phases in twisted bilayer transition metal dichalcogenides, *Nature materials* **19**, 861 (2020).

[28] D. M. Kennes, M. Claassen, L. Xian, A. Georges, A. J. Millis, J. Hone, C. R. Dean, D. Basov, A. N. Pasupathy, and A. Rubio, Moiré heterostructures as a condensed-matter quantum simulator, *Nature Physics* **17**, 155 (2021).

[29] C. Jin, Z. Tao, T. Li, Y. Xu, Y. Tang, J. Zhu, S. Liu, K. Watanabe, T. Taniguchi, J. C. Hone, *et al.*, Stripe phases in WSe₂/WS₂ moiré superlattices, *Nature Materials* **1** (2021).

[30] X. Huang, T. Wang, S. Miao, C. Wang, Z. Li, Z. Lian, T. Taniguchi, K. Watanabe, S. Okamoto, D. Xiao, *et al.*, Correlated insulating states at fractional fillings of the WS₂/WSe₂ moiré lattice, *Nature Physics* **17**, 715 (2021).

[31] Z. Chu, E. C. Regan, X. Ma, D. Wang, Z. Xu, M. I. B. Utama, K. Yumigeta, M. Blei, K. Watanabe, T. Taniguchi, *et al.*, Nanoscale conductivity imaging of correlated electronic states in WSe₂/WS₂ moiré superlattices, *Physical review letters* **125**, 186803 (2020).

[32] H. Pan, F. Wu, and S. D. Sarma, Quantum phase diagram of a Moiré-Hubbard model, *Physical Review B* **102**, 201104 (2020).

[33] N. Morales-Durán, A. H. MacDonald, and P. Potasz, Metal-insulator transition in transition metal dichalcogenide heterobilayer moiré superlattices, *Physical Review B* **103**, L241110 (2021).

[34] Y. Zhang, T. Liu, and L. Fu, Electronic structures, charge transfer, and charge order in twisted transition metal dichalcogenide bilayers, *Physical Review B* **103**, 155142 (2021).

[35] Z. Biand L. Fu, Excitonic density wave and spin-valley superfluid in bilayer transition metal dichalcogenide, *Nature communications* **12**, 1 (2021).

[36] H. Li, S. Li, E. C. Regan, D. Wang, W. Zhao, S. Kahn, K. Yumigeta, M. Blei, T. Taniguchi, K. Watanabe, *et al.*, Imaging generalized wigner crystal states in a WSe₂/WS₂ moiré superlattice, *arXiv preprint arXiv:2106.10599* (2021).

[37] M. Angel and A. H. MacDonald, Γ valley transition metal dichalcogenide moiré bands, *Proceedings of the National Academy of Sciences* **118** (2021).

[38] F. Wu, T. Lovorn, and A. H. MacDonald, Topological exciton bands in moiré heterojunctions, *Physical review letters* **118**, 147401 (2017).

[39] F. Wu, T. Lovorn, and A. MacDonald, Theory of optical absorption by interlayer excitons in transition metal dichalcogenide heterobilayers, *Physical Review B* **97**, 035306 (2018).

[40] H. Yu, G.-B. Liu, J. Tang, X. Xu, and W. Yao, Moiré excitons: From programmable quantum emitter arrays to spin-orbit-coupled artificial lattices, *Science advances* **3**, e1701696 (2017).

[41] K. Tran, G. Moody, F. Wu, X. Lu, J. Choi, K. Kim, A. Rai, D. A. Sanchez, J. Quan, A. Singh, *et al.*, Evidence for moiré excitons in van der Waals heterostructures, *Nature* **567**, 71 (2019).

[42] C. Jin, E. C. Regan, A. Yan, M. I. B. Utama, D. Wang, S. Zhao, Y. Qin, S. Yang, Z. Zheng, S. Shi, *et al.*, Observation of moiré excitons in WSe₂/WS₂ heterostructure superlattices, *Nature* **567**, 76 (2019).

[43] K. L. Seyler, P. Rivera, H. Yu, N. P. Wilson, E. L. Ray, D. G. Mandrus, J. Yan, W. Yao, and X. Xu, Signatures of moiré-trapped valley excitons in MoSe₂/WSe₂ heterobilayers, *Nature* **567**, 66 (2019).

[44] E. M. Alexeev, D. A. Ruiz-Tijerina, M. Danovich, M. J. Hamer, D. J. Terry, P. K. Nayak, S. Ahn, S. Pak, J. Lee, J. I. Sohn, *et al.*, Resonantly hybridized excitons in moiré superlattices in van der Waals heterostructures, *Nature* **567**, 81 (2019).

[45] N. Zhang, A. Surrente, M. Baranowski, D. K. Maude, P. Gant, A. Castellanos-Gomez, and P. Plochocka, Moiré intralayer excitons in a MoSe₂/MoS₂ heterostructure, *Nano letters* **18**, 7651 (2018).

[46] Y. Shimazaki, I. Schwartz, K. Watanabe, T. Taniguchi, M. Kroner, and A. Imamoğlu, Strongly correlated electrons and hybrid excitons in a moiré heterostructure, *Nature* **580**, 472 (2020).

[47] L. Zhang, Z. Zhang, F. Wu, D. Wang, R. Gogna, S. Hou, K. Watanabe, T. Taniguchi, K. Kulkarni, T. Kuo, *et al.*, Twist-angle dependence of moiré excitons in WS₂/MoSe₂ heterobilayers, *Nature communications* **11**, 1 (2020).

[48] H. Baek, M. Brotons-Gisbert, Z. Koong, A. Campbell, M. Rambach, K. Watanabe, T. Taniguchi, and B. D. Gerardot, Highly energy-tunable quantum light from moiré-trapped excitons, *Science advances* **6**, eaba8526 (2020).

[49] D. A. Ruiz-Tijerina, I. Soltero, and F. Mireles, Theory of moiré localized excitons in transition metal dichalcogenide heterobilayers, *Physical Review B* **102**, 195403 (2020).

[50] E. Liu, E. Barré, J. van Baren, M. Wilson, T. Taniguchi, K. Watanabe, Y.-T. Cui, N. M. Gabor, T. F. Heinz, Y.-C. Chang, *et al.*, Signatures of moiré trions in WSe₂/MoSe₂ heterobilayers, *Nature* **594**, 46 (2021).

[51] M. Brotons-Gisbert, H. Baek, A. Campbell, K. Watanabe, T. Taniguchi, and B. D. Gerardot, Moiré-trapped interlayer trions in a charge-tunable WSe₂/MoSe₂ heterobilayer, *arXiv preprint arXiv:2101.07747* (2021).

[52] H. Baek, M. Brotons-Gisbert, A. Campbell, K. Watanabe, T. Taniguchi, and B. D. Gerardot, Optical read-out of Coulomb staircases in a moiré superlattice via trapped interlayer trions, *arXiv preprint arXiv:2102.01358* (2021).

[53] S. Brem, C. Linderalv, P. Erhart, and E. Malic, Tunable phases of moiré excitons in van der Waals heterostructures, *Nano letters* **20**, 8534 (2020).

[54] S. Shabani, D. Halbertal, W. Wu, M. Chen, S. Liu, J. Hone, W. Yao, D. N. Basov, X. Zhu, and A. N. Pasupathy, Deep moiré potentials in twisted transition metal dichalcogenide bilayers, *Nature Physics* **17**, 720 (2021).

[55] H. Li, S. Li, M. H. Naik, J. Xie, X. Li, J. Wang, E. Regan, D. Wang, W. Zhao, S. Zhao, *et al.*, Imaging moiré flat bands in three-dimensional reconstructed wse 2/ws 2 superlattices, *Nature materials* **1** (2021).

[56] E. Li, J.-X. Hu, X. Feng, Z. Zhou, L. An, K. T. Law, N. Wang, and N. Lin, Lattice reconstruction induced multiple ultra-flat bands in twisted bilayer WSe₂, *arXiv preprint arXiv:2103.06479* (2021).

[57] M. H. Naik and M. Jain, Ultraflatbands and shear soli-

tons in moiré patterns of twisted bilayer transition metal dichalcogenides, *Physical review letters* **121**, 266401 (2018).

[58] H. Guo, X. Zhang, and G. Lu, Shedding light on moiré excitons: A first-principles perspective, *Science advances* **6**, eabc5638 (2020).

[59] M. H. Naik, S. Kundu, I. Maity, and M. Jain, Origin and evolution of ultraflat bands in twisted bilayer transition metal dichalcogenides: Realization of triangular quantum dots, *Physical Review B* **102**, 075413 (2020).

[60] Z. Zhan, Y. Zhang, P. Lv, H. Zhong, G. Yu, F. Guinea, J. Á. Silva-Guillén, and S. Yuan, Tunability of multiple ultraflat bands and effect of spin-orbit coupling in twisted bilayer transition metal dichalcogenides, *Physical Review B* **102**, 241106 (2020).

[61] I. Maity, P. K. Maiti, H. Krishnamurthy, and M. Jain, Reconstruction of moiré lattices in twisted transition metal dichalcogenide bilayers, *Physical Review B* **103**, L121102 (2021).

[62] S. Kundu, I. Maity, R. Bajaj, H. Krishnamurthy, and M. Jain, Atomic reconstruction and flat bands in strain engineered transition metal dichalcogenide bilayer moiré systems, *arXiv preprint arXiv:2108.01112* (2021).

[63] A. Wojs and P. Hawrylak, Negatively charged magnetoexcitons in quantum dots, *Physical Review B* **51**, 10880 (1995).

[64] V. Halonen, T. Chakraborty, and P. Pietiläinen, Excitons in a parabolic quantum dot in magnetic fields, *Physical Review B* **45**, 5980 (1992).

[65] W. Que, Excitons in quantum dots with parabolic confinement, *Physical Review B* **45**, 11036 (1992).

[66] P. Maksym and T. Chakraborty, Quantum dots in a magnetic field: Role of electron-electron interactions, *Physical review letters* **65**, 108 (1990).

[67] H. Yu, G.-B. Liu, P. Gong, X. Xu, and W. Yao, Dirac cones and Dirac saddle points of bright excitons in monolayer transition metal dichalcogenides, *Nature communications* **5**, 1 (2014).

[68] M. Glazov, T. Amand, X. Marie, D. Lagarde, L. Bouet, and B. Urbaszek, Exciton fine structure and spin decoherence in monolayers of transition metal dichalcogenides, *Physical Review B* **89**, 201302 (2014).

[69] T. Yu and M. Wu, Valley depolarization due to intervalley and intravalley electron-hole exchange interactions in monolayer MoS₂, *Physical Review B* **89**, 205303 (2014).

[70] F. Wu, F. Qu, and A. H. MacDonald, Exciton band structure of monolayer MoS₂, *Physical Review B* **91**, 075310 (2015).

[71] A. Kormányos, G. Burkard, M. Gmitra, J. Fabian, V. Zólyomi, N. D. Drummond, and V. Falko, $k \cdot p$ theory for two-dimensional transition metal dichalcogenide semiconductors, *2D Materials* **2**, 022001 (2015).

[72] J. Gu, L. Ma, S. Liu, K. Watanabe, T. Taniguchi, J. C. Hone, J. Shan, and K. F. Mak, Dipolar excitonic insulator in a moiré lattice, *arXiv preprint arXiv:2108.06588* (2021).